J Adv Ceram

Research Article

Unravelling the H_2O-assisted high-pressure sintering mechanism: A route to highly transparent cubic alumina ceramics

Xingtao Chen[1,✉], Yijun Shen[1], Zhouru Kong[1], Qinbiao Nan[1], Dahan Liu[1], Lixin Yu[1,✉], Jun Wang[2], Jianqi Qi[3], Tiecheng Lu[3]

Cite this article: Chen X, Shen Y, Kong Z, et al. *J Adv Ceram* 2026, **15**(5): 9221291. https://doi.org/10.26599/JAC.2026.9221291

ABSTRACT: Transparent cubic alumina (γ-Al_2O_3) ceramics are promising optical materials but are challenging to densify without phase transformation or cracking. Herein, we report a novel H_2O-assisted high-pressure sintering (HPS) strategy that enables the fabrication of highly transparent, crack-free γ-Al_2O_3 ceramics at temperatures as low as 300 °C. By combining GPa-level pressures (0.8–5 GPa) with precisely controlled H_2O concentrations (5–75 wt%) as a transient solvent, we achieve near-theoretical densities (> 99%) and exceptional optical transmittance (> 80% in the visible range). Systematic investigation reveals a non-monotonic dependence of densification and transparency on H_2O content, with an optimal concentration of ~15 wt% under 5 GPa. Microstructural and spectroscopic analyses correlate superior optical quality with a pore-free, nanocrystalline microstructure and the absence of secondary phases. Crucially, through integrated first-principles calculations and *ab initio* molecular dynamics simulations, we unravel the atomic-scale mechanism. Namely, under high pressure, H_2O dissociates at the particle interface, with the resultant H^+ forming Al–H bonds and OH^- incorporating into interstitial lattice sites. This process stabilizes a hydroxyl-cubic aluminate (HAl_2O_4)-like structure, which not only facilitates stress-free densification via an enhanced dissolution–precipitation pathway but also effectively relieves internal stresses that typically cause cracking in pressure-only sintering. This work provides a fundamental mechanistic understanding of the synergistic role of H_2O and ultra-high pressure in low-temperature ceramic consolidation, establishing a generalizable route to transparent nanocrystalline ceramics that are otherwise inaccessible via conventional thermal sintering.

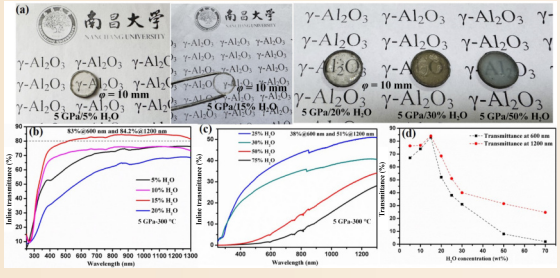

KEYWORDS: γ-Al_2O_3; transparent ceramics; transient liquid phase; high-pressure sintering; optical properties

1 Introduction

Transparent ceramic materials have garnered significant interest for advanced optical applications, including laser gain media, infrared windows, and transparent armor, owing to their superior mechanical strength, thermal stability, and tailored optical properties compared with conventional glasses and single crystals [1–3]. Among various transparent ceramics, alumina is a prime candidate due to its high hardness, excellent chemical inertness, and broad spectral transmission range. While α-Al_2O_3 is a widely used transparent ceramic, its hexagonal crystal structure introduces birefringence, which causes optical scattering at grain boundaries and limits its transparency, especially in thicker components [4,5]. This has spurred interest in cubic alumina polymorphs, such as γ-Al_2O_3. As γ-Al_2O_3 possesses a cubic crystal structure, it is optically isotropic and theoretically capable of achieving high transparency without scattering losses from birefringence [6]. The necessity and application potential of such transparent cubic alumina ceramics are considerable. They combine the excellent mechanical strength, high-temperature resistance, and chemical durability of alumina with optical clarity. This unique property makes them highly desirable for advanced applications, including solid-state lighting, transparent armor, missile domes, infrared windows, and gain media. However, its metastable nature means it easily transforms to α-Al_2O_3 at high temperatures. Conventional processing is therefore challenging, as it must achieve near-full densification to eliminate pores while avoiding this phase transformation [7]. Therefore, the fabrication of fully dense and transparent γ-Al_2O_3 bulk ceramics necessitates a sintering approach that operates at drastically reduced temperatures while effectively driving densification.

[1] School of Physical and Materials Science, Nanchang University, Nanchang 330031, China. [2] School of Physics and Electronic Engineering, Jiangsu Normal University, Xuzhou 221116, China. [3] College of Physics, Sichuan University, Chengdu 610064, China.

✉ Corresponding authors. E-mail: X. Chen, chenxingtao@ncu.edu.cn; Lixin Yu, yulixin@ncu.edu.cn

Received: February 11, 2026; Revised: March 31, 2026; Accepted: April 1, 2026

In response to these challenges, the cold sintering process (CSP) has emerged as a revolutionary low-temperature densification technique. CSP fundamentally redefines ceramic processing by utilizing a transient liquid phase (often water) in conjunction with uniaxial pressure to achieve densification at exceptionally low temperatures (typically < 400 °C) [8,9]. The core mechanism of CSP is a dissolution–precipitation process. Under applied pressure, the solid particles experience increased solubility at their contact points in the presence of the liquid phase, leading to dissolution. Mass transport then occurs through the liquid medium, and precipitation takes place in pore regions, driving densification without the need for high thermal energy. This mechano–chemistry coupling effect effectively replaces the thermal diffusion that drives conventional sintering, allowing for the consolidation of ceramics while suppressing grain growth, minimizing volatile element loss, and enabling the co-sintering of materials with vastly different thermal properties. The technique holds immense promise for developing novel functional materials with enhanced performance and reduced energy consumption. Recently, applied to γ-Al_2O_3, CSP has yielded translucent ceramics, yet the reported optical transmittance remains modest (e.g., < 20% in the visible range) under moderate pressures (300–500 MPa) [10,11]. This limitation is primarily attributed to insufficient densification and residual pores, suggesting that the driving force provided by conventional CSP may be inadequate for achieving optical-grade γ-Al_2O_3 transparent ceramics. On the other hand, ultra-high pressure (GPa-level) sintering has demonstrated the ability to densify ceramics at low temperatures by drastically reducing kinetic barriers [12,13]. In a prior study, we reported the successful preparation of highly transparent γ-Al_2O_3 ceramics with average grain sizes below 20 nm via ultrahigh-pressure (5 GPa) sintering without additives [14]. These studies establish that the combination of pressure can overcome the kinetic barriers to densification while suppressing the phase transformation from γ-Al_2O_3 to α-Al_2O_3. However, ultrahigh-pressure-only sintering at low temperature often introduces considerable internal stress, leading to sample cracking and compromising the integrity, and it typically requires subsequent high-temperature annealing that risks phase transformation [15–17].

A critical yet unresolved question thus arises: Can the beneficial effects of a transient liquid (as in CSP) and ultra-high pressure be synergistically combined to achieve full densification of γ-Al_2O_3 at low temperatures while simultaneously mitigating internal stress and preserving the cubic phase for optimal transparency? Moreover, the specific role of the most common and economical transient liquid water in such a high-pressure regime remains fundamentally unclear. While water is known to facilitate mass transport in CSP, its behavior and chemical interaction with the ceramic matrix under GPa-level pressures are poorly understood, leaving a gap in the mechanistic foundation needed to rationally design such processes.

In this work, we address these challenges by developing and investigating an H_2O-assisted high-pressure sintering route for fabricating highly transparent γ-Al_2O_3 nanocrystalline ceramics. Contrary to prior studies on the detrimental effect of water on transparency in cubic alumina, this study reveals that water can, in fact, alleviate internal stresses and improve structural integrity. We systematically explore the effects of H_2O content and pressure on the densification, microstructure, and optical transmittance. More importantly, we employ a combination of advanced microscopy, spectroscopy, and multiscale computational simulations to unravel the atomic-scale mechanism by which H_2O operates under high pressure. We reveal how water dissociation and the subsequent incorporation of hydroxyl species into the alumina lattice not only enhance densification kinetics but also act as a structural modifier to relieve stress and stabilize the transparent cubic phase. This study, therefore, provides not only a novel processing pathway to high-performance transparent γ-Al_2O_3 but also a fundamental mechanistic understanding that could guide the low-temperature fabrication of other functional metastable ceramics.

2 Experimental

2.1 Fabrication procedure

The γ-Al_2O_3 nanopowders were prepared as described in a previous study [14]. Prior to sintering, the prepared powders were freeze-dried at −50 °C for 24 h under vacuum (< 0.1 mbar) to remove residual solvents while minimizing particle agglomeration. The freeze-dried powders were sealed in a vacuum quartz tube and then calcined at 600 °C in air for 2 h to remove residual moisture and obtain pure γ-Al_2O_3 nanopowders. Calcination was performed at a heating rate of 2 °C/min to ensure uniform thermal treatment and controlled phase evolution. For the CSP, pure γ-Al_2O_3 nanopowders were mixed with H_2O solutions of varying concentrations and ground to form a homogeneous paste. For each experiment, the desired amount of deionized water (5, 10, 25, 50, and 75 wt% relative to the powder weight) was added to the γ-Al_2O_3 powders and processed in the glove box. The mixture was homogenized by manual grinding in an agate mortar for 15 min to obtain a uniform paste. To minimize water evaporation prior to sintering, the paste was immediately transferred to the die and encapsulated within 2 min of mixing. Control experiments confirmed that water loss during this handling period was < 3.5% of the added water. All water contents reported in this study refer to the nominal added amounts. The mixture was divided into two portions. The first portion was processed using a conventional CSP setup. A circular heated mold (Shanghai Jingsheng Scientific Instrument Co., Ltd., China) made of hot-die steel with an inner diameter of 16 mm was employed. The mixture was transferred into the mold and pressed manually under a uniaxial pressure ranging from 300 to 800 MPa. Sintering was conducted at temperatures between 100 and 300 °C for 40 min. After sintering, the obtained samples were dried in an oven at 80 °C to remove residual moisture.

The second portion of the mixture was densified via a high-pressure route. The powders were initially uniaxially cold-pressed into cylindrical green pellets (φ = 12 mm, $h \approx 4$ mm) and processed in a glove box. These pellets were typically wrapped in gold foil and then sealed in a flexible rubber mold to prevent infiltration of the pressing medium and ensure that all added water remained within the green body. Subsequently, they are subjected to cold isostatic pressing at 200 MPa to improve their homogeneity and green density prior to high-pressure sintering. Each pellet was then placed inside a hexagonal boron nitride (h-BN) capsule, which was inserted into a graphite tube heater. High-pressure sintering was performed using a Kawai-type multi-anvil apparatus with a Walker-type module (mavo press LPR 1000–400/50; Max Voggenreiter GmbH, Germany). Experiments were conducted at pressures of 5 GPa and temperatures below 350 °C. For the 5.0 GPa runs, an 18/14 assembly was used. In a typical high-pressure high-temperature cycle, the pressure was first raised to 5.0 GPa. The sample was then heated to the set temperature of 300 °C by applying an electric current and held for 40 min. Finally, the samples were quenched by cutting off the power, followed by slow decompression to ambient pressure.

During the high-pressure experiments, the temperature in the sample chamber was monitored directly using a PtRh6%–PtRh30% (type-B) thermocouple placed adjacent to the sample. The pressure was calibrated *in situ* by employing the well-established phase transitions of Bi (2.55 GPa), Tl (3.67 GPa), and Ba (5.5 GPa) as internal references.

The pressures of 0.8 and 5 GPa were selected as fixed conditions to investigate two distinct densification regimes. The 5 GPa condition was chosen based on prior work demonstrating that γ-Al_2O_3 achieves high density (~99%) at 5 GPa while retaining its nanocrystalline structure. The 0.8 GPa condition represents the upper range of conventional cold sintering pressures, allowing investigation of water-assisted mechanisms under conditions where dissolution–precipitation remains dominant. Fixing pressure within each series enabled systematic evaluation of H_2O concentration and temperature effects without the confounding influence of pressure variation.

2.2 Characterization and analysis

The phase composition of the synthesized powders and sintered ceramics was analyzed by an X-ray diffractometer (XRD; D/max-rA, Rigaku, Japan) using Ni-filtered Cu Kα radiation (λ = 0.15406 nm). The average crystallite size of the ceramics was estimated from XRD peak broadening using the Scherrer equation: $D = K\lambda/(\beta\cos\theta)$, where K is the shape factor (0.94), λ is the X-ray wavelength, β is the full width at half maximum (in radians) after instrumental correction, and θ is the Bragg angle. The bulk density of the sintered ceramics was measured via the Archimedes method with deionized water as the immersion medium. Microstructural characterization was conducted using a scanning electron microscope (SEM; S-4800, Hitachi, Japan) on pristine fracture surfaces and a transmission electron microscope (TEM; JEM-2500SE, JEOL, Japan) on powder samples and focused-ion-beam-thinned ceramic cross-sections. The average grain size was statistically determined by manually measuring over 100 grains from SEM micrographs using ImageJ software. The in-line optical transmittance of polished ceramic disks was measured from the ultraviolet to the near-infrared (IR) range (250–2500 nm) using a spectrophotometer (Lambda-750, Perkin-Elmer, USA) equipped with an integrating sphere.

2.3 Computational methods

To elucidate the atomic-scale mechanism of H_2O in the cold sintering process, first-principles calculations and *ab initio* molecular dynamics (AIMD) simulations were performed. All calculations were based on density functional theory (DFT) as implemented in the Vienna *Ab initio* Simulation Package (VASP). The projector augmented-wave (PAW) method was employed to describe electron–ion interactions, and the Perdew–Burke–Ernzerhof (PBE) generalized gradient approximation was used for the exchange–correlation functional. A plane-wave cutoff energy of 520 eV was applied. The cubic γ-Al_2O_3 model was constructed based on the defective spinel structure (space group $Fd\bar{3}m$), containing 56 atoms in a conventional cell. A 2×2×1 supercell was used to model the (100) surface, where a vacuum layer of 15 Å was added to avoid periodic interactions (Eq. (1)).

$$E_{ads} = E_{slab+H_2O} - E_{slab} - E_{H_2O} \quad (1)$$

where E_{slab+H_2O} is the total energy of the slab with an adsorbed H_2O molecule, E_{slab} is the energy of the clean slab, and E_{H_2O} is the energy of an isolated H_2O molecule in a large box. The climbing-image nudged elastic band (CI-NEB) method was used to determine the minimum-energy pathways and activation barriers for H_2O dissociation and subsequent H/OH migration.

AIMD simulations were carried out in the canonical (NVT) ensemble using a Nosé–Hoover thermostat to control the temperature. A time step of 1 fs was used. The system was subjected to a constant pressure of 5 GPa via the Parrinello–Rahman barostat. Simulations were run at three representative temperatures: 273 K (representing the initial mixing state), 573 K (near the onset of significant mass transport), and 773 K (approaching the upper limit of our cold sintering window). Each trajectory was propagated for at least 10 ps after equilibration. The atomic trajectories, coordination numbers, and key bond lengths (Al–O, Al–H, and O–H) were analyzed to track the structural evolution and formation of the hydroxyl-stabilized phase.

3 Results and discussion

3.1 Powder analysis

To investigate the effect of calcination temperature on the phase composition and particle size, we first examined the phase evolution of the as-synthesized precursors. Figure 1 shows the phase and morphology of the synthesized γ-Al_2O_3 powders. XRD patterns (Figs. 1(a) and 1(b)) reveal the phase evolution with calcination temperature from 500 to 1200 °C for 4 h. The patterns of powders calcined at 500, 600, 700, and 900 °C show diffraction peaks that can be indexed to cubic $Al_{2/3}Al_2O_4$ (γ-Al_2O_3, JCPDS #77-0403; lattice parameters $a = b = c$ = 0.7906 nm), indicating that a single-phase γ-Al_2O_3 can be obtained within the 500–900 °C range, as shown in Fig. 1. As the temperature increases to 1200 °C, the diffraction pattern shifts toward that of hexagonal α-Al_2O_3 (JCPDS #99-0036), demonstrating the transformation from face-centered cubic γ-Al_2O_3 to the thermodynamically stable α-Al_2O_3 phase. SEM images (Figs. 1(c) and 1(d)) reveal that the γ-Al_2O_3 powders consist of fine aggregates of nanosized primary particles. The average particle size was further estimated from SEM analysis (Fig. 1(c)), and the average particle size of the γ-Al_2O_3 powders was ~13.6 nm, which agrees well with the mean particle size of approximately 12 nm derived from TEM analysis (Fig. 1(d)). TEM images further reveal that the powders consist of weakly agglomerated primary particles connected through fine necks, indicating a narrow particle-size distribution within the powder. The selected area electron diffraction pattern of γ-Al_2O_3 powders inserted in Fig. 1(d) exhibits clear and continuous polycrystalline rings that can be indexed to the (111), (220), and (400) planes of face-centered cubic γ-Al_2O_3. This demonstrates that the sample consists of randomly oriented nanocrystalline grains, and the γ-phase remains stably retained after low-temperature sintering. These results confirm that the synthesized γ-Al_2O_3 powder possesses fine, uniform particle characteristics, which are essential for achieving effective compaction and subsequent densification during sintering.

3.2 Densification and microstructure

While transparent γ-Al_2O_3 has been obtained via additive-free ultra-high-pressure (5 GPa) sintering at 300 °C [14], the role of sintering aids in the high-pressure sintering process remains unclear. Therefore, in this study, we also systematically investigated how additives and sintering temperature influence the microstructure and optical quality of γ-Al_2O_3 ceramics. Figure 2 illustrates the influence of key processing parameters on the densification of γ-Al_2O_3 ceramics via the high-pressure sintering route. As shown in Fig. 2(a), the relative density exhibits a clear dependence on the concentration of the H_2O additive. At a lower

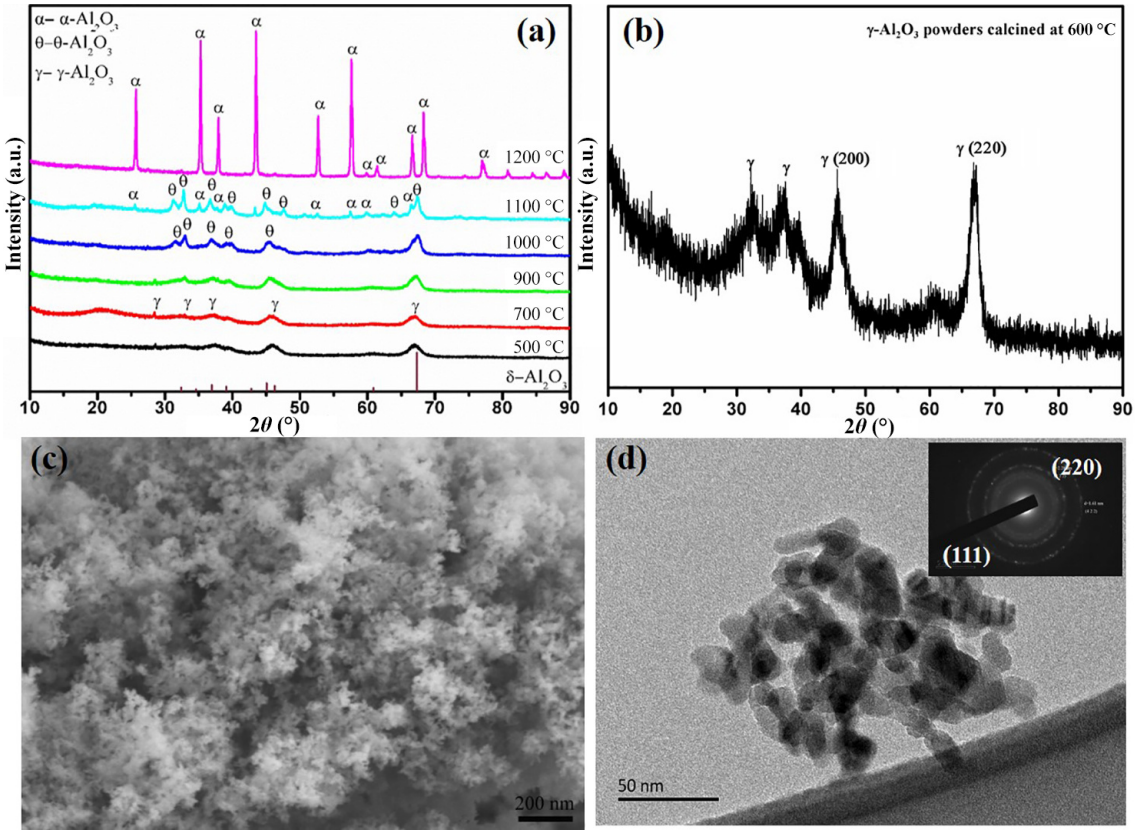

Fig. 1 (a, b) XRD patterns of γ-Al_2O_3 powders calcined at various temperatures (500–1200 °C). (c) SEM and (d) TEM images of γ-Al_2O_3 powders synthesized via a homogeneous-precipitation route and calcined at 600 °C. Inset: corresponding selected area electron diffraction pattern of γ-Al_2O_3 powders.

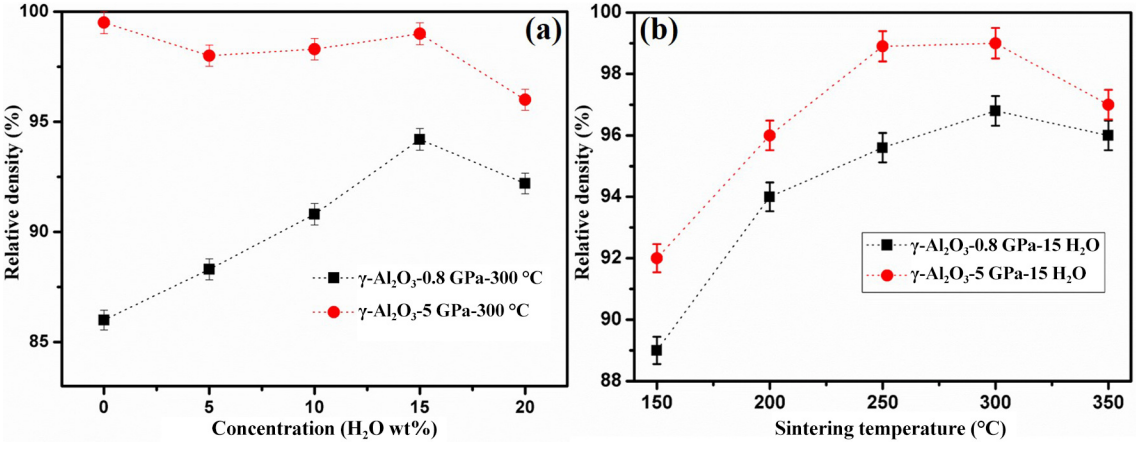

Fig. 2 Relative density of high-pressure sintered γ-Al_2O_3 as a function of (a) H_2O concentration and (b) sintering temperature under applied pressures of 0.8 and 5 GPa.

pressure of 0.8 GPa, the relative density initially increases with H_2O content, reaching a maximum with a relative density of 94% at an optimal concentration of 15 wt%, beyond which further addition leads to a decline. Although the 800-MPa pressure used in this study is higher than typical cold sintering conditions (< 500 MPa), the relatively modest density achieved at 800 MPa in our work, combined with the clear role of water in promoting densification, confirms that this is indeed a cold sintering process rather than traditional high-pressure compaction. The nonlinear relationship between pressure and density observed here is consistent with the cold sintering process, which emphasizes that pressure primarily enables particle rearrangement, while the dissolution–precipitation mechanism is driven by the transient liquid phase. When the pressure is increased to 5 GPa, the densification behavior shows a significant improvement and a distinct dependence on H_2O content. Notably, even without any additive, a relative density of 99.5% is achieved under 5 GPa, highlighting the dominant role of high pressure in driving consolidation [14]. Upon introducing H_2O, the density initially exhibits a slight decrease at low concentrations (up to ~5 wt%). Beyond this point, it rises steadily and reaches a maximum of approximately 99% at an optimal H_2O content of 15 wt%. A further increase in H_2O concentration, however, results in a gradual decline in density. This non-monotonic trend indicates that while an appropriate amount of H_2O enhances mass transport and promotes full densification, an excessive amount may hinder the process, likely due to residual porosity or microstructural coarsening induced by overwetting. While the

sample without H_2O achieves a relative density of 99%, these samples consistently exhibited macroscopic cracking upon decompression in the early work [14,17]. This cracking renders them unsuitable for further characterization or practical applications. In contrast, samples prepared with 15 wt% H_2O achieve comparable density (98.8%–99.1%) while maintaining complete structural integrity without visible cracks (Fig. 7). In addition, the densification behavior observed at 5 GPa in this study should be distinguished from conventional cold sintering. While water addition at this pressure appears to assist particle rearrangement and may promote localized dissolution at contact points, the primary densification mechanism likely involves plastic deformation and pressure-induced phenomena. At extreme pressure, the role of water shifts from being the primary enabler of mass transport to being an auxiliary agent that facilitates particle sliding and may enhance grain boundary diffusion without fundamentally altering the pressure-dominated densification process. The contrasting behaviors at 800 MPa and 5 GPa in our study illustrate this mechanistic transition. At 800 MPa, the densification shows characteristics consistent with cold sintering, in which water appears to play an active role in promoting densification, although an optimal density was not achieved. At 5 GPa, water still contributes to particle rearrangement, but the extreme pressure likely activates additional deformation mechanisms that dominate the densification process, as evidenced by the phase-pure γ-Al_2O_3 compaction, which parallels the pressure-induced sintering pathway [14]. The significant enhancement in densification underscores the critical role of high pressure in overcoming kinetic barriers, even at low temperatures. The effect of sintering temperature is presented in Fig. 2(b). Under both 0.8 and 5 GPa, the relative density increases progressively with temperature from 100 to 300 °C. This trend is attributed to the enhanced atomic mobility and accelerated dissolution–precipitation kinetics at elevated temperatures [18]. Notably, the density values achieved at 5 GPa are consistently higher than those at 0.8 GPa across the entire temperature range, reaffirming the synergistic effect of pressure and temperature in promoting densification. The combined analysis of Figs. 2(a) and 2(b) identifies an optimal processing route characterized by a specific H_2O concentration and a sintering temperature near 300 °C under 5-GPa pressure for achieving near-theoretical density in γ-Al_2O_3 via high-pressure sintering.

High-pressure sintered γ-Al_2O_3 with 15 wt% H_2O at 300 °C and 0.8 GPa also achieved > 90% theoretical density. The distinct densification effect of using H_2O as a liquid aid can also be directly observed from the fracture surfaces of bulk samples. Figure 3 presents the fracture-surface morphologies of γ-Al_2O_3 ceramics sintered at 0.8 GPa with varying H_2O contents. A clear evolution in microstructure is observed with increasing H_2O concentrations. At low H_2O contents (5–10 wt%, Figs. 3(a) and 3(b)), the fracture surface exhibits a relatively porous and granular appearance, which is consistent with its relatively low density of only 86% (Fig. 2(a)), indicating that water-assisted densification is limited under these conditions. Interparticle boundaries remain visible, suggesting limited particle rearrangement and insufficient mass transport under these conditions. As the H_2O content increased to 15 wt% (Fig. 3(c)), the microstructure improved significantly, with a marked reduction in porosity and the formation of distinct sintering necks between particles. Correspondingly, the relative density increased to 94% (Fig. 2(a)). The fracture surface becomes much denser and more cohesive, with a noticeable reduction in visible pores. This correlation suggests that an appropriate amount of water effectively eliminates large pores and promotes particle rearrangement by facilitating the dissolution–precipitation process. However, when the water content is further increased to 25 wt% (Fig. 3(d)), although the density remains at 90.2%, localized particle clustering is observed (indicated by arrows), which is consistent with the mechanism by which excessive water leads to local supersaturation and independent precipitation. Further increasing the H_2O content to 50 wt% (Fig. 3(e)) leads to the reappearance of microstructural inhomogeneity. Some regions remain dense, while others show evidence of particle clustering or localized overwetting, which may act as defects. At the highest H_2O content of 75 wt% (Fig. 3(f)), the microstructure becomes visibly coarser and less uniform, with distinct flaky regions and possible signs of abnormal grain growth. These morphological trends correlate well with the density data presented in Fig. 2(a). The optimal microstructure observed at ~15 wt% H_2O corresponds to the peak in relative density, confirming that this composition provides the best balance between solvent-assisted mass transport and pore removal under the applied pressure of 0.8 GPa. Overall, water acted as a transient liquid phase, enhancing particle rearrangement and mass transport without significant grain growth.

Figure 4(a) presents the XRD patterns of γ-Al_2O_3 ceramics high-pressure sintered at 0.8 GPa with varying H_2O contents. All patterns exhibit characteristic diffraction peaks that can be indexed to the cubic γ-Al_2O_3 phase (JCPDS #77-0403), confirming that the low-temperature cold sintering process successfully preserves the metastable cubic structure without transformation to the α-phase. A clear trend is observed with increasing H_2O content from 15 to 25 wt%: The diffraction peaks become broader and weaker. This indicates a decrease in crystallinity as the transient liquid phase content rises. However, a key observation is that the sample with the highest H_2O content (e.g., 75 wt%) shows peak intensities and widths similar to those of the sample with 25 wt% H_2O. This suggests that beyond a certain optimal threshold, further increasing the H_2O content does not promote additional crystallization or grain growth. The stagnation in peak evolution may be attributed to the saturation of the dissolution–precipitation process, where excess H_2O no longer accelerates ion transport, and the increased porosity or microstructural inhomogeneity at very high H_2O contents, as observed in SEM (Fig. 3), which can offset the crystallinity improvement. Notably, no secondary phases (hydroxides or α-Al_2O_3) are detected, confirming that H_2O acts as a sintering aid without introducing crystalline impurities under these conditions. The absence of the α-Al_2O_3 phase in all patterns underscores the effectiveness of the cold sintering route in suppressing the high-temperature phase transformation at low pressure.

Figure 4 also presents the optical performance and visual appearance of γ-Al_2O_3 ceramics high-pressure sintered at 0.8 GPa with varying H_2O contents. The transmittance spectra in Fig. 4(b) reveal a strong correlation between H_2O content and optical quality across both the visible and IR ranges. Samples with a thickness (t) of 2 mm prepared with low H_2O contents (≤ 10 wt%) exhibit relatively low transmittance, particularly in the visible region, which is consistent with the porous microstructures observed in Figs. 3(a) and 3(b). The transmittance increases significantly for the sample containing 15 wt% H_2O, reaching a maximum value of 63% at 600 nm and ~70% at 1200 nm. This optimum coincides with the densification and most uniform microstructure shown in Figs. 2 and 3(c). At higher H_2O contents (> 15 wt%), the transmittance decreases notably, especially in the shorter-wavelength region, indicating enhanced scattering likely caused by residual porosity and microstructural inhomogeneity.

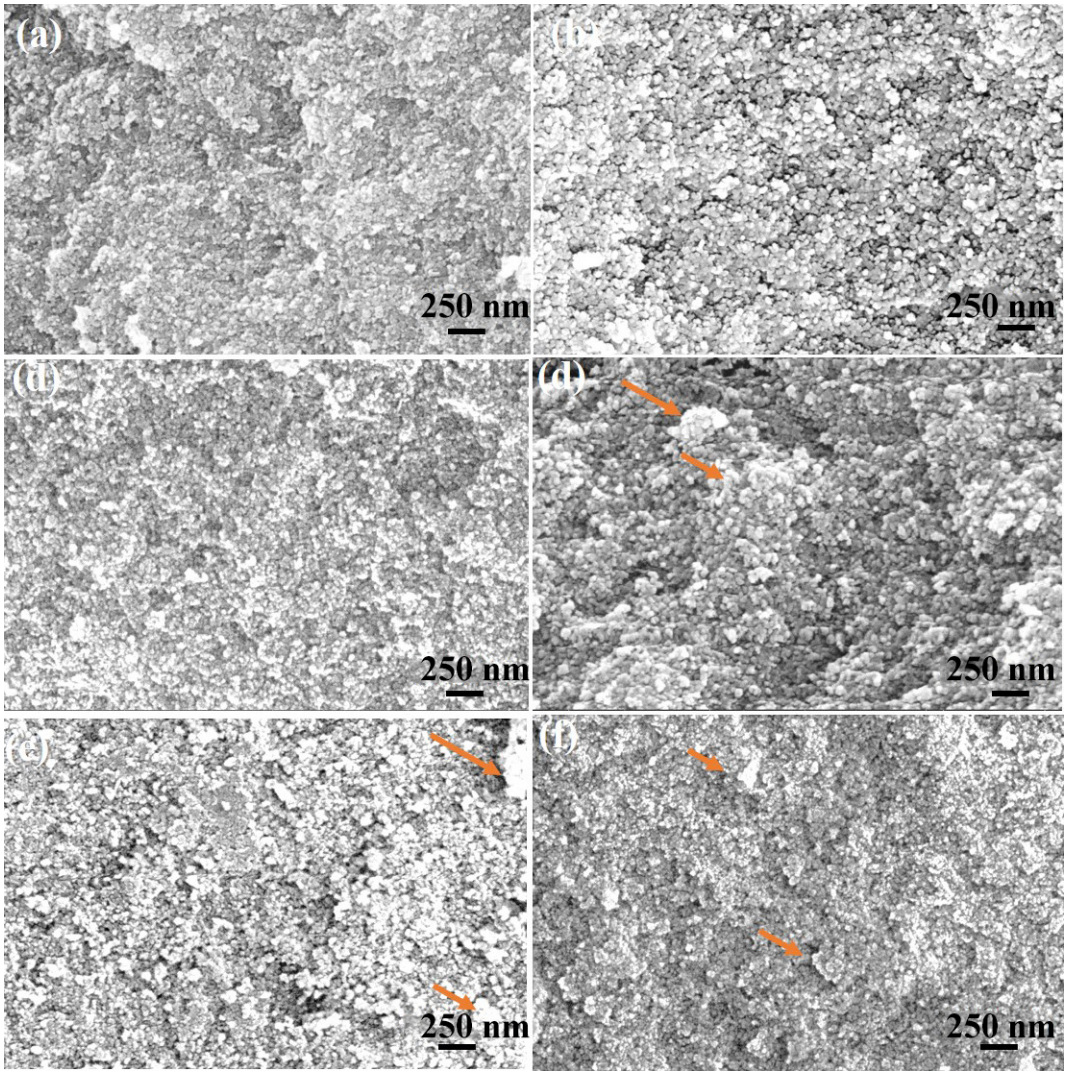

Fig. 3 SEM images of fractured surfaces of γ-Al_2O_3 ceramics high-pressure sintered at 0.8 GPa with different H_2O contents: (a) 5 wt%, (b) 10 wt%, (c) 15 wt%, (d) 25 wt%, (e) 50 wt%, and (f) 75 wt%.

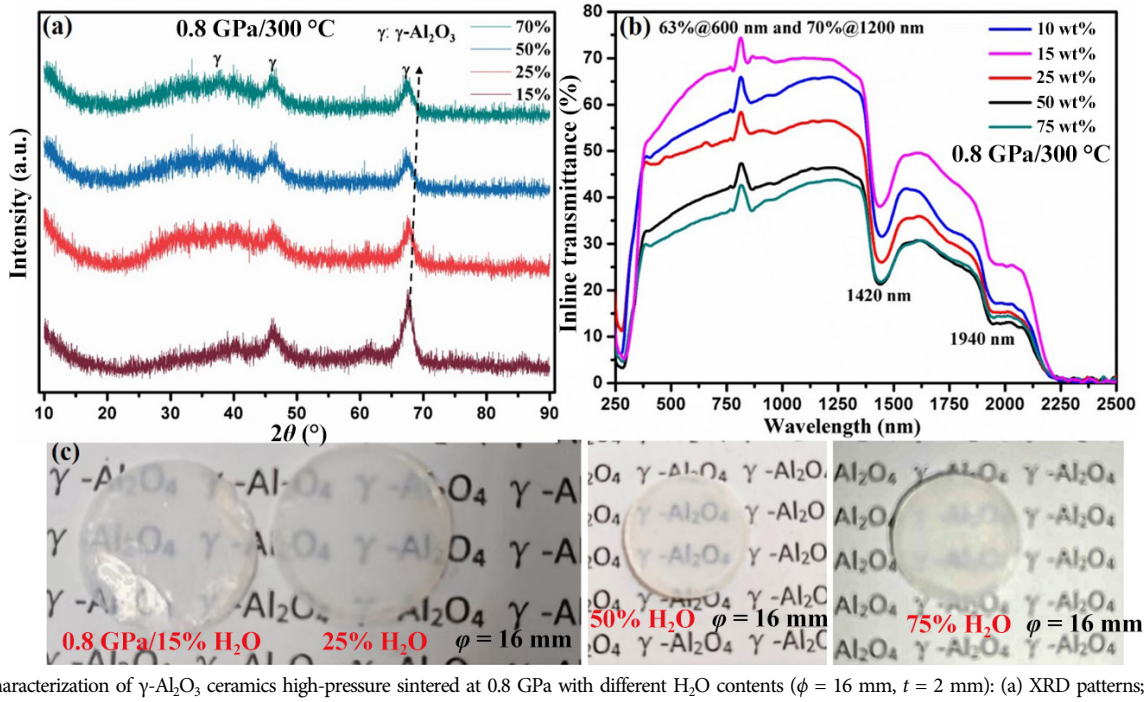

Fig. 4 Characterization of γ-Al_2O_3 ceramics high-pressure sintered at 0.8 GPa with different H_2O contents (ϕ = 16 mm, t = 2 mm): (a) XRD patterns; (b) optical transmittance spectra across visible and infrared wavelengths; and (c) corresponding photographs.

In a recent work, a translucent ceramic with in-line transmittance reaching 16% at approximately 800 nm was obtained via cold-pressing γ-Al_2O_3 ceramics with NaOH solutions instead of H_2O [10]. In our work, the high-pressure sintered samples (0.8 GPa) exhibited high transmittance (60% at 600 nm), comparable to conventionally sintered γ-Al_2O_3 ceramics with NaOH solutions due to the introduction of NaOH as a second phase. The absence of large pores and secondary phases contributed to the optical clarity. Two characteristic absorption peaks at approximately 1420 and 1940 nm are observed in the transmittance spectra of all samples doped with H_2O. The absorption in these samples is much greater than that in the sample without H_2O additions [14,19]. The presence of hydroxyl absorption peaks in the infrared spectra and the decrease in infrared transmittance can be directly attributed to the nanocrystalline microstructure coupled with our processing route. The high interfacial area inherent to nanoceramics provides a vast reservoir for adsorbing and retaining the H_2O used as a transient solvent. While this solvent is essential for facilitating low-temperature densification via the cold sintering process, a fraction of the hydroxyl species inevitably remains trapped at grain boundaries or within the lattice after sintering. Thus, the infrared transparency becomes a sensitive indicator of the trade-off between utilizing H_2O for densification and minimizing its residual incorporation—a balance that is optimized at the 15 wt% H_2O concentration in our study. This interfacial amplification effect underscores that achieving full densification must be balanced with stringent control of impurity incorporation and distribution at the nanoscale in fabricating nanocrystalline transparent ceramics for broadband optical applications. Similar phenomena have been observed in other transparent nanocrystalline ceramics, such as Y_2O_3–MgO [19] and $MgAl_2O_4$ [20].

The photographs in Fig. 4(c) provide a direct visual confirmation of these trends. The sample with 15 wt% H_2O appears highly transparent, with clear visibility of the background text, whereas samples with higher H_2O contents show increasing levels of haze and opacity. The progressive loss of clarity beyond the optimal H_2O concentration is visually consistent with the deterioration in both microstructure (Fig. 3) and measured transmittance (Fig. 4(b)). The optical transmittance spectra shown in Fig. 4(a) not only reflect the overall transparency but also encode information about the dominant scattering mechanisms. The pronounced decrease in transmittance at shorter wavelengths (e.g., < 600 nm) for samples with non-optimal H_2O contents suggests the presence of Rayleigh-type scattering, which scales inversely with the fourth power of the wavelength [21]. This behavior is characteristic of scattering centers significantly smaller than the wavelength of light, such as nanosized residual pores within the ceramic matrix. The correlation is substantiated by the SEM observations in Fig. 3, where samples with low (5–10 wt%) or high (≥ 35 wt%) H_2O contents exhibit higher porosity or microstructural inhomogeneity, respectively. To quantitatively assess the contribution of forward versus diffuse scattering, optical haze can be estimated from the transmittance data. The haze (H), defined as the ratio of diffuse transmittance ($T_{diffuse}$) to total transmittance (T_{total}), can be approximated for highly transparent ceramics using Eq. (2) [22]:

$$H \approx 1 - T_{direct}/T_{total} \quad (2)$$

where T_{direct} is the in-line transmittance. Although direct measurement of $T_{diffuse}$ was not performed, the significant drop in T_{direct} at short wavelengths for off-optimal samples implies a concurrent rise in haze, confirming that scattering is the primary cause of transparency loss. The sample with 15 wt% H_2O, which exhibits the highest and flattest transmittance curve across the visible spectrum, corresponds to the minimal haze. Furthermore, the presence of the absorption peaks at 1420 and 1940 nm, attributed to hydroxyl groups, introduces an additional wavelength-dependent loss mechanism in the infrared region. In all samples, their relative intensity may vary with H_2O content and sintering pressure, subtly influencing the near-IR transmittance baseline. A complete deconvolution of absorption and scattering losses would require complementary measurement of the absorption coefficient and direct haze quantification, which are planned for future work. Nevertheless, the current data unequivocally demonstrate that optimizing the H_2O content at 0.8 GPa effectively suppresses pore-mediated scattering, leading to a ceramic with optical quality suitable for both visible and near-infrared window applications. These results collectively demonstrate that an optimal H_2O content (~15 wt%) at 0.8 GPa is critical to achieving high optical transparency in cold-sintered γ-Al_2O_3, effectively balancing the solvent-assisted densification benefit against the optical degradation effects of the excess liquid phase. Beyond aluminum oxide systems, cold sintering has proven effective for fabricating transparent materials from other precursors. Kang *et al.* [23] recently demonstrated that transparent SiO_2 glass with a relative density of 96.8% and a transmittance of ~80% in the visible region could be fabricated at only 200 °C using H_2SiO_3 as transient chemistry. Notably, they observed a glass-to-ceramic transition between 200 and 300 °C, with recrystallization producing ~150-nm α-quartz grains and enhanced mechanical properties. This parallels our observation of γ-Al_2O_3 formation at 300 °C without the need for higher temperatures and suggests that transient hydroxide phases enable particle rearrangement and mass transport at similarly low temperatures.

The optical transmittance of ceramics sintered at 0.8 GPa, even with the optimal H_2O content (~15 wt%), has not reached the theoretical value (> 80% in the visible region). This performance gap can be primarily ascribed to their suboptimal relative density, indicating that the driving force provided by 0.8-GPa pressure alone is insufficient to achieve full densification and complete pore removal. Figure 5 displays the XRD patterns of γ-Al_2O_3 ceramics consolidated by sintering at an ultrahigh pressure of 5 GPa, with H_2O content varying across a wide range from 5 to 75 wt%. The patterns are presented in two panels to clearly distinguish the trends in lower (Fig. 5(a)) and higher (Fig. 5(b)) concentration regimes. All samples exclusively show the characteristic diffraction peaks of the cubic γ-Al_2O_3 phase when the H_2O content ranges from 5 to 20 wt%, as shown in Fig. 5(a). No traces of the stable α-Al_2O_3 phase or any aluminum hydroxide phases are detected in those samples with low concentrations of H_2O (< 20 wt%). This confirms the exceptional phase stability afforded by the high-pressure cold sintering process, effectively locking in the metastable γ-phase at a temperature of only 300 °C. Figure 5(b) reveals a critical phase evolution for samples with H_2O contents above 25 wt% sintered at 5 GPa. When the H_2O concentration exceeds 25 wt%, both new diffraction peaks corresponding to $Al(OH)_3$ (gibbsite or bayerite) emerge, indicating the onset of a pressure-induced hydration reaction. This transformation becomes pronounced at 30 wt%, where several strong $Al(OH)_3$ peaks dominate the pattern, suggesting significant partial conversion of γ-Al_2O_3 to the hydroxide phase under these extreme conditions. A further compositional shift occurs at 50 wt% H_2O. The XRD pattern not only shows persistent $Al(OH)_3$ peaks but also exhibits a new, strong alumina diffraction peak near $2\theta \approx 75°$.

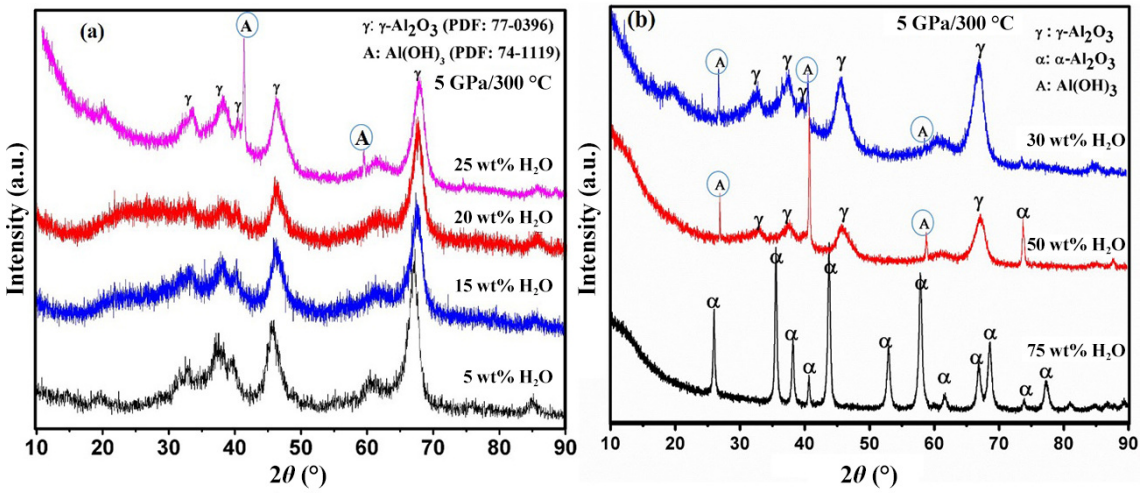

Fig. 5 XRD patterns of γ-Al_2O_3 ceramics cold sintered at 5 GPa with different H_2O contents, displayed in two concentration ranges: (a) 5–25 wt% and (b) 30–75 wt%.

This peak is consistent with the (300) plane of θ-Al_2O_3 or the (113) plane of α-Al_2O_3, marking the beginning of a dehydration-induced transition back to a more stable alumina polymorph during or after sintering [24]. Most strikingly, at the highest content of 75 wt% H_2O, the pattern undergoes a complete transformation. All diffraction peaks are exclusively indexed to the hexagonal α-Al_2O_3 phase, with no residual traces of γ-Al_2O_3 or $Al(OH)_3$. This indicates that an over-critical amount of H_2O under high pressure drives a full sequence of phase transformations: γ-Al_2O_3→$Al(OH)_3$→α-Al_2O_3. The observed phase transformation with increasing H_2O content from 5 to 75 wt% at 5 GPa and 300 °C can be understood through a combination of pressure-induced nucleation and water-accelerated mass transport. In a previous study [25], high-pressure sintering studies on γ-Al_2O_3 demonstrated that applied pressure at 200 MPa enables γ-Al_2O_3 to α-Al_2O_3 transformation at 500–800 °C, lower than ambient-pressure transformation through stress-induced nucleation at particle contact points. At our significantly higher pressure of 5 GPa, these stress concentrations are dramatically amplified, creating abundant high-energy nucleation sites that lower the kinetic barrier for phase transformation. However, pressure alone is insufficient because the transformation only proceeds at high H_2O contents (≥ 50 wt%), indicating that water plays an essential catalytic role. Under ultrahigh pressure, trapped water exists as a supercritical hydrothermal medium with enhanced solubility for Al^{3+} species and accelerated diffusion kinetics [26]. This high-pressure aqueous phase enables rapid dissolution of γ-Al_2O_3 at particle surfaces and transport of dissolved species to growing nuclei. Similar water-accelerated transformation has been observed in aqueous phase reforming conditions, where γ-Al_2O_3 converts to boehmite (AlOOH) at only 200 °C in liquid water, suggesting that under our extreme conditions, water-mediated reactions are dramatically accelerated. The ultrahigh pressure favors a denser α-Al_2O_3 phase, while the abundant water promotes hydration reactions. The final phase observed in our high-H_2O samples likely represents the outcome of this competition between pressure-driven densification and water-driven hydration, potentially yielding a nanocomposite or partially transformed structure. This pathway is fundamentally different from direct thermal transformation and highlights the unique hydrothermal-like chemistry enabled by the combination of excess water and ultra-high pressure.

Figure 6 presents a comprehensive microstructural and chemical analysis of the γ-Al_2O_3 ceramic high-pressure sintered at 5 GPa using 15 and 20 wt% H_2O as the transient liquid phase. The SEM image in Fig. 6(a) reveals a dense, pore-free fracture surface with uniform grain distribution, confirming the high densification achieved under these conditions. The microstructure exhibits near-spherical grains with an average size of 27 nm, as illustrated in Fig. 6(a). This is further corroborated by the high-resolution TEM (HRTEM) images in Figs. 6(b)–6(d), which show well-defined nanocrystallites with clear lattice fringes. The measured interplanar spacings with the lattice pattern of (111) correspond to the cubic γ-Al_2O_3 phase, as shown in Fig. 6(d). The sharp grain boundaries indicate a minimal amorphous intergranular phase, which is a key factor for high transparency. Figures 6(e) and 6(f) display the energy-dispersive X-ray spectroscopy (EDS) spectra acquired from selected regions. The spectra confirm that the material is primarily composed of aluminum and oxygen, with no detectable impurity peaks, affirming the high chemical purity of the sintered ceramic. A weak signal possibly corresponding to Fe was observed in the EDS spectra near the detection limit. The corresponding elemental maps in Figs. 6(g) and 6(h) visualize the distribution of Al (Fig. 6(h)) and O (Fig. 6(g)). These maps demonstrate a homogeneous and uniform distribution of elements at the nanoscale, with no evidence of elemental segregation or secondary phase formation. The absence of Al- or O-deficient regions, combined with the dense microstructure observed in SEM and HRTEM images, provides a direct structural explanation for the superior optical transparency (Fig. 7). The grain boundaries appear sharp and narrow, typically no more than 1–2 atomic layers in width, with no detectable amorphous film or secondary phase. This clean boundary structure minimizes optical scattering at interfaces, directly contributing to the high transmittance in the visible range. Moreover, the absence of continuous amorphous phases suggests that the residual H_2O or hydroxyl species, which are inevitable in aqueous-assisted sintering, are likely incorporated into the γ-Al_2O_3 lattice as point defects or form isolated clusters rather than wetting the grain boundaries [27]. This defect configuration is beneficial for optical homogeneity. Closer inspection of the HRTEM images reveals the presence of occasional lattice distortions and point-defect clusters (e.g., in Fig. 6(c)). These features can be attributed to the accommodation of hydroxyl groups or to the slight non-stoichiometry inherent to the spinel-type γ-Al_2O_3 structure. Such defect complexes can act as scattering centers at specific wavelengths, which may correlate with the minor absorption features observed in the transmittance spectra, as shown in Fig. 7.

Quantitatively, the density of these point defects can be estimated from the EDS spectra (Figs. 6(e) and 6(f)) by analyzing the fine structure of the O–K edge or through electron energy-loss spectroscopy in future work, linking defect concentration directly to optical absorption coefficients. In summary, the atomic-scale characterization confirms that the H_2O-assisted, high-pressure sintering route not only achieves full densification but also produces a nanocrystalline structure with coherent grain boundaries. This unique microstructure is the fundamental reason why the ceramic simultaneously exhibits high optical transmittance, low optical scatter, and promising mechanical integrity.

Figure 6 also displays the microstructural and chemical characteristics of the γ-Al_2O_3 ceramic high-pressure sintered at 5 GPa using 20 wt% H_2O as the transient liquid phase. Compared with the sample with 15 wt% H_2O (Fig. 6), distinct differences

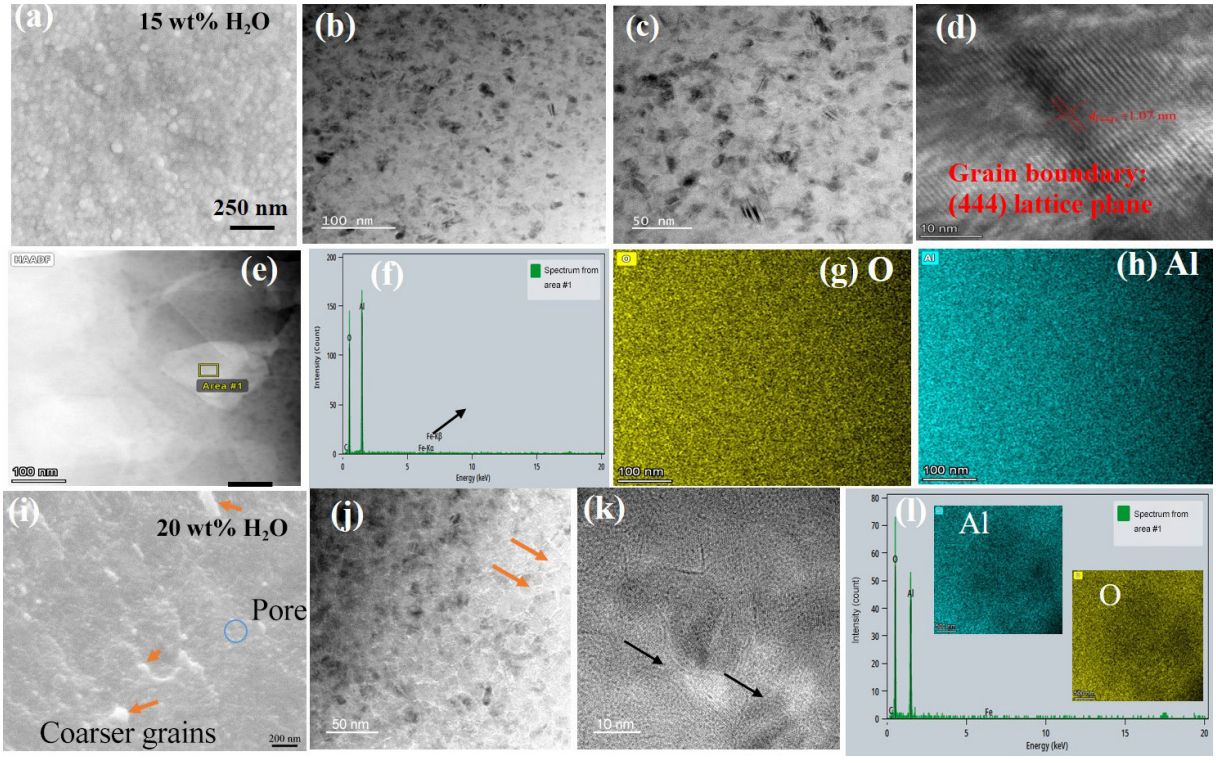

Fig. 6 Microstructural and chemical characterization of cold-sintered γ-Al_2O_3 ceramics at 5 GPa using 15 wt% and 20 wt% H_2O as the liquid phase. For samples with 15 wt% H_2O: (a) SEM image; (b–d) HRTEM images; (e, f) EDS spectra; (g, h) corresponding EDS elemental maps. For samples with 20 wt% H_2O: (i) SEM image; (j, k) HRTEM images; (l) EDS spectra (with inset showing corresponding EDS elemental maps).

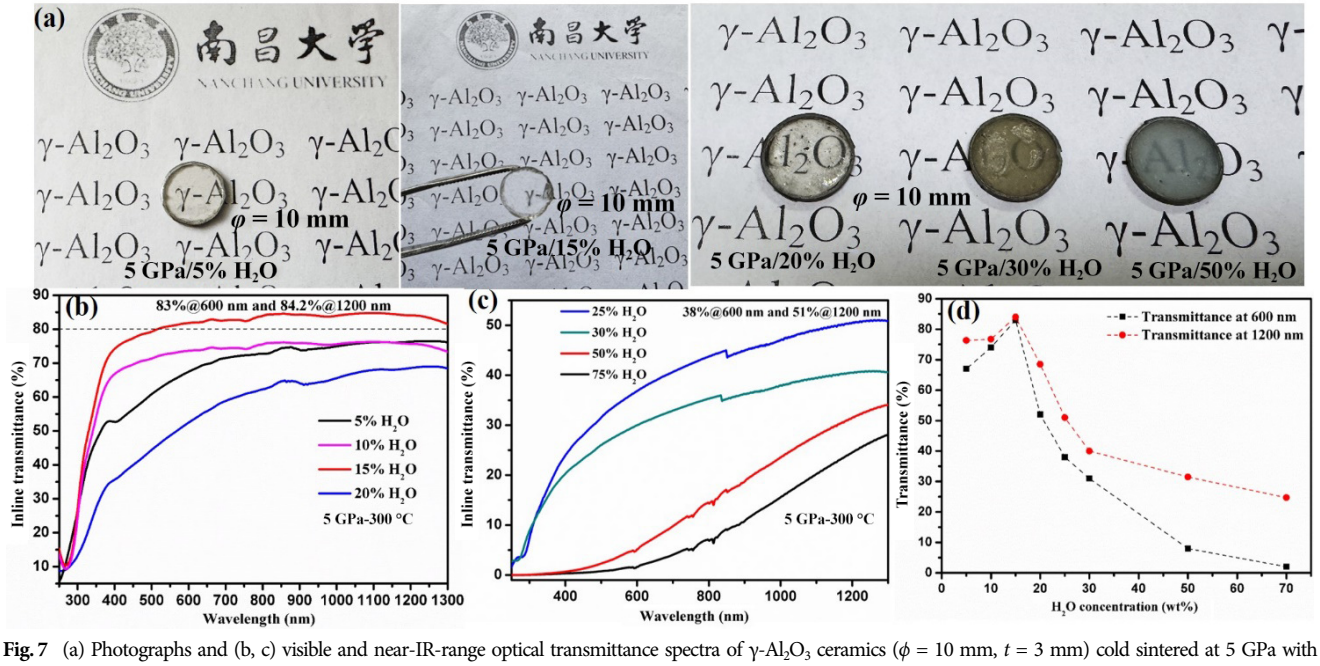

Fig. 7 (a) Photographs and (b, c) visible and near-IR-range optical transmittance spectra of γ-Al_2O_3 ceramics (ϕ = 10 mm, t = 3 mm) cold sintered at 5 GPa with different H_2O contents. (d) Optical transmittance (at wavelengths of 600 and 1200 nm) of cold-sintered γ-Al_2O_3 as a function of H_2O concentration.

emerge. The SEM image in Fig. 6(i) shows a fracture surface that exhibits localized regions of slightly coarser grains (indicated by arrows) and sporadic micropores (indicated by circles). This subtle inhomogeneity suggests that excess liquid phase may lead to uneven grain growth or incomplete pore removal during the final stage of sintering. The HRTEM images in Figs. 6(j)–6(k) provide more revealing insights at the nanoscale. Although clear lattice fringes of γ-Al_2O_3 are observed, the grain boundaries appear less defined than those in Fig. 6(c). In some areas (e.g., Fig. 6(j)), a disordered interfacial layer is visible, which may correspond to a residual amorphous phase or a hydroxyl-enriched region. This interfacial film likely originates from the incomplete expulsion or decomposition of the excess H_2O-derived species. Such an intergranular phase can act as a potent scattering center for visible light, directly explaining the reduced transmittance and increased haze observed for this composition (Fig. 7). Additionally, a higher density of point-defect clusters and lattice distortions within the grains is noticeable, as shown in Fig. 6(k), consistent with the incorporation of excess hydroxyl groups into the lattice. The EDS spectrum in Fig. 6(l) confirms that the bulk composition remains predominantly aluminum and oxygen, with no foreign cationic impurities detected. The corresponding elemental maps visualize the distribution of Al and O. These maps demonstrate a homogeneous and uniform distribution of both elements at the nanoscale, with no evidence of elemental segregation or secondary phase formation in the whole. The microstructural features in Fig. 6 collectively elucidate the mechanism behind the performance degradation when H_2O content exceeds the optimal value: Excess liquid leads to microstructural coarsening, promotes the formation of grain boundary phases, and increases point-defect density, all of which detrimentally affect optical transparency. However, the presence of the amorphous intergranular film and point defects, which are below the spatial resolution and sensitivity limits of standard EDS, underscores the need for techniques with higher chemical sensitivity (such as electron energy-loss spectroscopy) to precisely quantify the oxygen-to-aluminum ratio and identify hydrogen-related species in these critical regions.

Figure 7 presents a comparative analysis of the visual and spectroscopic optical properties for γ-Al_2O_3 ceramics sintered under a high pressure of 5 GPa with varying H_2O contents. The photographs in Fig. 7(a) provide an immediate, qualitative assessment of transparency. A clear trend is evident: Ceramics prepared with an intermediate H_2O content (5–20 wt%, as shown in Fig. 7(a)) exhibit superior visual clarity, allowing the underlying text or pattern to be seen distinctly. More significantly, all the γ-Al_2O_3 ceramics sintered by using H_2O as a sintering aid do not crack and are completely uniform compared with the sample fabricated via an applied pressure of 5 GPa without using H_2O [14,28]. In contrast, samples with excessive H_2O, such as 30 or 50 wt%, as shown in Fig. 7(a), display noticeable haze or opacity, correlating with suboptimal microstructures and phase transformation. In addition, a light-yellow tint is observed in the sample containing 30 wt% H_2O, as visible in Fig. 7(a). This coloration is a direct indicator of the formation of color centers within the material, which are commonly attributed to the aggregation of oxygen vacancies or other point defects or the $Al(OH)_3$ second phase that introduces subbandgap energy levels. This qualitative observation is quantitatively confirmed by the visible and near-IR-range transmittance spectra in Figs. 7(b) and 7(c). The spectra corresponding to the optically clear sample show a high and flat transmittance profile, exceeding 80% across most of the visible spectrum (500–1300 nm). Notably, the γ-Al_2O_3 ceramic sample exhibits the highest optical quality, with transmittance reaching a maximum of 83% at a wavelength of 600 nm and 84.2% at a wavelength of 1.2 μm; these values approach those determined for commercial sapphire single crystals (86% transmittance of ultraviolet to visible and infrared light). This indicates minimal absorption and scattering losses, achieved through effective pore elimination and a homogeneous nanocrystalline matrix. Conversely, the spectra for the hazy sample with either 30 or 50 wt% H_2O reveal a significantly lower transmittance, particularly at shorter wavelengths (< 800 nm), due to the emergence of the second phase (Fig. 5). The phase mixtures typically scatter light and reduce transmittance, while complete transformation to a single phase (either α-Al_2O_3 or a hydrated phase) could improve transparency if fully dense. The steep decline toward the blue region is characteristic of Rayleigh scattering, caused by residual nanosized defects such as pores [22]. The influence of H_2O concentration on the optical quality of high-pressure sintered γ-Al_2O_3 is quantitatively compared at two representative wavelengths: 600 nm in the visible region and 1200 nm in the near-infrared region, as plotted in Fig. 7(d). The transmittance at both wavelengths follows a similar non-monotonic trend with H_2O content, but with key differences that elucidate the dominant scattering mechanisms. At the optimal H_2O content of ~15 wt%, the transmittance reaches its maximum at both wavelengths, achieving values of 83% at 600 nm and 84% at 1200 nm. This simultaneous high performance across the visible and near-IR confirms that the ceramic obtained under these conditions has a highly homogeneous, pore-limited microstructure (Fig. 6), with minimal absorption and scattering losses. For H_2O-deficient samples (< 10 wt%), the transmittance is slightly reduced at both wavelengths, but is consistently lower at 600 nm than at 1200 nm. This wavelength dependence is characteristic of Rayleigh scattering from residual nanoscale pores, the intensity of which scales as $I \propto \lambda^{-4}$. The stronger scattering at shorter wavelengths directly indicates that the primary optical limitation in these samples is sub-optimal densification, leaving behind a population of fine pores. In the samples with 20 wt% H_2O, a distinct behavior emerges. Although the transmittance decreases from its optimal value, the ratio of T_{600nm}/T_{1200nm} shows an even more pronounced decline. This suggests that in addition to residual porosity, a second scattering mechanism stemming from the formation of larger grains or defect clusters becomes significant, as shown in Fig. 6. Additionally, the characteristic hydroxyl absorption near 1400–1500 nm may begin to influence the baseline at 1200 nm, contributing to the drop in optical performance. In H_2O-excess samples (> 25 wt%), the transmittance further decreases relative to the optimum. This is attributed to the emergence of a second phase that becomes quite significant. The direct correspondence between visual appearance and spectroscopic data conclusively establishes H_2O content as a decisive factor for optimizing both optical quality and residual stress state, even under the potent driving force of 5 GPa. These findings highlight a critical synergy that, while high pressure is essential for achieving densification, precise regulation of the transient H_2O phase is paramount to attaining superior transparency and a stress-relieved microstructure in nanocrystalline γ-Al_2O_3 ceramics. Therefore, this work clarifies that the synergy between pressure and a precisely controlled transient liquid phase is the cornerstone for fabricating high-integrity, transparent nanocrystalline γ-Al_2O_3 ceramics.

3.3 Introduction to structural models and key simulation findings

The precise crystal structure of γ-Al_2O_3, a key catalyst support, remains a subject of debate, particularly regarding the positions of

Al^{3+} cations and vacancies. Three primary structural models have been proposed [29,30]: (i) a defective spinel model (γ-$Al_{2/3}Al_2O_4$) in which all cations occupy spinel sites with cation vacancies maintaining charge balance; (ii) a hydrogen-stabilized model (γ-HAl_2O_4) where protons occupy nonspinel interstitial sites to compensate for charge; and (iii) models that propose a nonspinel arrangement altogether. To further clarify the role of H_2O in modifying the structure of γ-Al_2O_3 under high-pressure sintering conditions, we performed first-principles density functional theory calculations and *ab initio* molecular dynamics simulations on a cubic γ-Al_2O_3 model. A water molecule was introduced into the periodic supercell to simulate the atomic-scale interaction during sintering. Figure 8 presents first-principles and molecular dynamics simulation results that elucidate the atomic-scale mechanism of H_2O as a transient liquid phase during the high-pressure sintering of γ-Al_2O_3. Figure 8(a) shows the DFT-calculated stable adsorption configurations of a H_2O molecule on low-index γ-Al_2O_3 surfaces. The calculations reveal that H_2O preferentially chemisorbs at under-coordinated Al sites, with one O–H bond pointing toward a surface oxygen, facilitating proton transfer. The energy profile in Fig. 8(b) quantifies the critical steps following adsorption. The energy barrier for H_2O dissociation into adsorbed H^+ and OH^- is significantly reduced under the simulated high-pressure (5 GPa) condition compared with ambient pressure. Furthermore, the migration barriers for the dissociated H and OH species along the surface or into interstitial sites are also lowered, providing a thermodynamic and kinetic rationale for the enhanced mass transport observed experimentally. Figures 8(c)–8(e) display snapshots from *ab initio* molecular dynamics simulations at 5 GPa and increasing temperatures (273, 573, and 773 K). At 273 K (Fig. 9(c)), H_2O remains largely molecular and mobile on the particle surfaces. As the temperature rises to 573 K (Fig. 8(d)), corresponding to the onset of our sintering process, widespread dissociation of H_2O occurs. The adsorbed H_2O molecule readily dissociates under the simulated high-pressure conditions. The liberated H^+ species rapidly adsorb onto adjacent aluminum atoms, forming transient Al–H bonds, while OH^- groups incorporate into interstitial sites within the alumina lattice. At 773 K (Fig. 8(e)), this process is complete, leading to a reconstructed interface where hydroxyl groups are integrated into the alumina lattice, effectively forming a hydroxyl-stabilized structure similar to HAl_2O_4, as inferred from the calculation result [6,31]. The analysis of bond-length and coordination-number evolutions (not shown in a separate panel but derived from the AIMD trajectories) confirms this mechanism. The Al–O bond lengths in the presence of H and OH show slight distortion and a trend toward higher average coordination, indicating lattice relaxation and stress relief. This atomic-scale picture directly explains the dual role of H_2O. First, H_2O as a dissociative solvent drastically lowers the energy barriers for surface and bulk diffusion, enabling densification at low temperatures. Second, H_2O, as a chemical modifier, is incorporated into the lattice, passivates defects, and relieves internal stress, thereby yielding a dense ceramic with high optical quality. These simulations provide a fundamental theoretical foundation for the optimal H_2O concentration (15 wt%) identified experimentally, beyond which excess hydroxylation may lead to defect clustering and performance degradation. Therefore, our computational results support the hydrogen-stabilized model (γ-HAl_2O_4) as the dominant structural modifier when γ-Al_2O_3 is processed with H_2O under high pressure. The incorporation of hydroxyl groups into interstitial sites not only explains the observed structural stability at low temperatures but also provides an atomic-scale mechanism for the stress relief and optical transparency enhancement achieved in our experiments.

3.4 Mechanism analysis

Figure 9 schematically illustrates the proposed mechanism of H_2O-

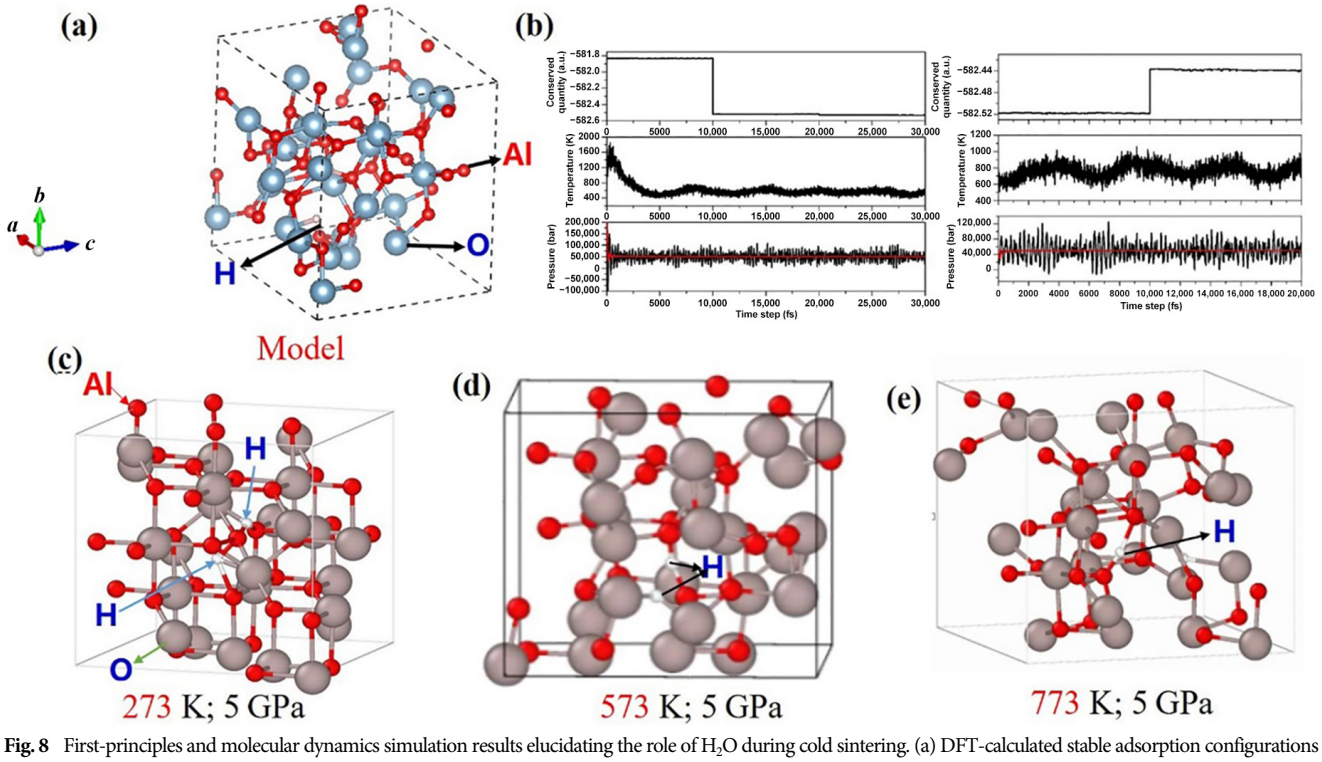

Fig. 8 First-principles and molecular dynamics simulation results elucidating the role of H_2O during cold sintering. (a) DFT-calculated stable adsorption configurations of H_2O on γ-Al_2O_3 surfaces; (b) energy profiles for H_2O dissociation and H/OH migration; AIMD-simulated atomic trajectories under 5-GPa pressure at (c) 273 K, (d) 573 K, and (e) 773 K. Evolution of key bond lengths and coordination numbers during sintering process.

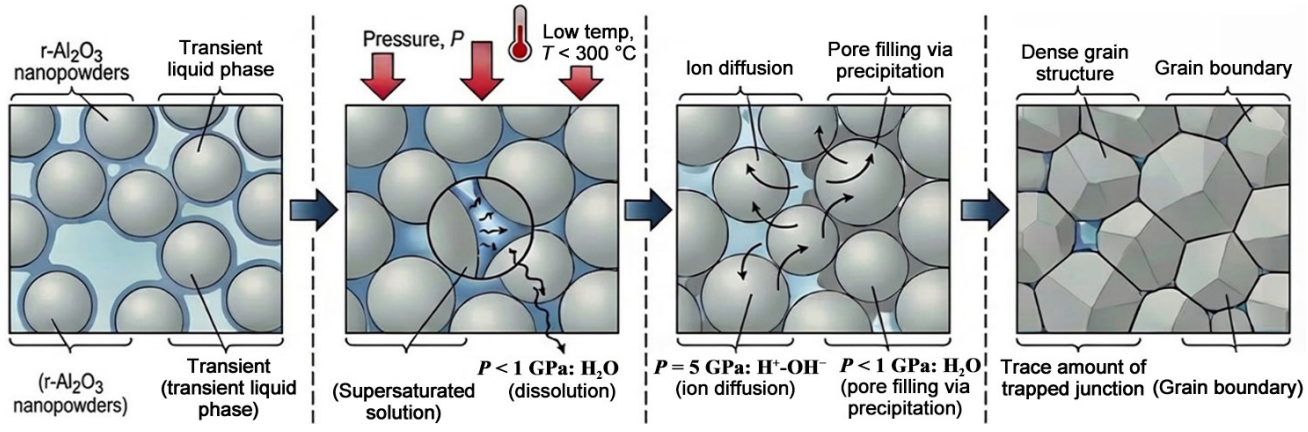

Fig. 9 Mechanism of high-pressure sintering for γ-Al_2O_3 ceramics with H_2O additives.

assisted high-pressure sintering for γ-Al_2O_3 transparent ceramics. The process can be described in three key stages. First, upon mixing, H_2O molecules adsorb onto the surfaces of γ-Al_2O_3 nanoparticles, preferentially at under-coordinated Al sites. Under relatively low pressure (0.8 GPa or below), the applied stress is insufficient to fully activate the dissociation of H_2O molecules into mobile H^+ and OH^- species. Consequently, densification in this regime is predominantly governed by a pressure-enhanced dissolution–precipitation process, where the transient aqueous phase facilitates mass transport without extensive chemical modification of the alumina lattice [32]. Under high applied pressure (5 GPa) and low temperature (< 300 °C), a fraction of these H_2O molecules can dissociate into H^+ and OH^- species, creating a chemically active interfacial layer. Second, the applied pressure dramatically increases the solubility of the oxide surfaces in the nanoconfined aqueous phase. Aluminum ions dissolve from particle contact points (regions of high stress and chemical potential) into the transient liquid [33]. These ions then diffuse through the thin liquid film and reprecipitate at particle necks or pore surfaces (regions of lower chemical potential). This dissolution–diffusion–precipitation cycle, accelerated by pressure, is the core densification mechanism that occurs at temperatures far below those required for solid-state diffusion. As densification proceeds, the dissociated H^+ and OH^- species are incorporated into the growing ceramic lattice. Protons form local Al–H bonds, while hydroxyl groups occupy interstitial sites, effectively leading to the formation of a hydroxyl-stabilized cubic structure. This incorporation passivates defects and relieves local lattice strain, which is critical for preventing microcracking, which is a common issue in pressure-only sintering. The final microstructure is a dense, nanocrystalline ceramic with coherent grain boundaries and minimal residual stress. This mechanism explains the non-monotonic dependence of properties on H_2O content: Insufficient H_2O results in poor densification, high porosity, and a second phase; optimal H_2O content yields full density and high transparency; excess H_2O can lead to overwetting, microstructural coarsening, a second phase, and hydroxyl-related IR absorption, degrading optical performance.

4 Conclusions

In this study, we demonstrate that H_2O-assisted high-pressure sintering is a highly effective route for fabricating fully dense, transparent γ-Al_2O_3 nanocrystalline ceramics at temperatures as low as 300 °C. The key to success lies in the precise control of the H_2O content under GPa-level pressure. An optimal H_2O concentration of approximately 15 wt% under 5 GPa pressure yields ceramics with a relative density > 99% and excellent optical transmittance (> 84% in the visible range). In contrast, insufficient H_2O leads to incomplete densification, while excess H_2O promotes microstructural inhomogeneity, residual porosity, a second phase, and hydroxyl-related infrared absorption, all of which degrade optical quality. The fundamental role of H_2O extends beyond that of a conventional sintering aid. Our combined experimental and multiscale computational investigation reveals a dual mechanism. First, under high pressure, H_2O dissociates at the particle surfaces and significantly lowers the energy barriers for atomic diffusion and facilitates rapid mass transport via a dissolution–precipitation process, thereby enabling densification at low temperatures. Second, the dissociated protons and hydroxyl groups are incorporated into the alumina lattice. Protons form transient Al–H bonds, while hydroxyl groups occupy interstitial sites, leading to the formation of a hydroxyl-stabilized cubic structure akin to HAl_2O_4. This incorporation effectively passivates defects, relieves internal stresses that would otherwise cause cracking, and is responsible for the exceptional optical clarity of the final ceramic. This work resolves the longstanding practical challenge of co-achieving full densification and phase stability in metastable γ-Al_2O_3 without microcracking. It provides a clear mechanistic framework that redefines H_2O not merely as a processing aid but also as a crucial structural mediator in high-pressure sintering. The insights gained here establish a general material design principle that is likely applicable to the low-temperature fabrication of other metastable, nanocrystalline functional ceramics requiring high optical and mechanical performance.

This work demonstrates that water-assisted high-pressure processing enables low-temperature densification of γ-Al_2O_3 ceramics with controlled phase stability and microstructural evolution. The successful consolidation at 300 °C under ultrahigh pressure opens new possibilities for fabricating advanced ceramic materials that are challenging to process via conventional high-temperature sintering. Beyond the Al_2O_3 system investigated here, this water-assisted high-pressure approach holds promise for broader application in other ceramic systems, including solid electrolytes for all-solid-state batteries, where low-temperature processing can prevent elemental volatilization and enable co-sintering with electrode materials, piezoelectric ceramics such as $KNaNbO_3$ (KNN), where A-site element loss must be suppressed, and ceramic–polymer composites for functional devices requiring multimaterial integration without thermal degradation. Furthermore, the method's potential to produce ceramics with tailored porosity suggests applicability in filtration membranes, catalyst supports, and biomedical scaffolds. These preliminary

prospects highlight the translational value of this processing strategy for sustainable and energy-efficient ceramic manufacturing.

Acknowledgements

This study was supported by the National Natural Science Foundation of China (No. 52562018) and the Natural Science Foundation of Jiangxi Province, China (No. 20242BAB25105).

Author contributions

Xingtao Chen: writing – review & editing, writing – original draft, methodology, investigation, funding acquisition, conceptualization. Yijun Shen: writing – original draft, methodology, data curation. Zhouru Kong: methodology, investigation, formal analysis, data curation. Qinbiao Nan: investigation, formal analysis, data curation. Dahan Liu: formal analysis, data curation. Lixin Yu: formal analysis, writing – review & editing. Jun Wang: writing – review & editing. Jianqi Qi: writing – review & editing. Tiecheng Lu: writing – review & editing.

Availability of data and materials

The data that support the findings of this study are available from the corresponding author upon reasonable request.

Competing interests

The authors have no competing interests to declare that are relevant to the content of this article.

References

[1] Zhang P, Liu XY, Ji Y, *et al.* A high-crystallinity transparent glass-ceramic enables encapsulant-free, high quantum efficiency NIR-II miniature light source. *Adv Funct Mater* 2025, **36**: 30116.

[2] Jiang MD, Qu LJ, Tao Y, *et al.* 3D nanoprinting of multifunctional MgO transparent ceramics. *ACS Nano* 2025, **19**: 19318–19327.

[3] Mu Z, Kong KR, Jiang K, *et al.* Pressure-driven fusion of amorphous particles into integrated monoliths. *Science* 2021, **372**: 1466–1470.

[4] Ratzker B, Wagner A, Kalabukhov S, *et al.* Non-uniform microstructure evolution in transparent alumina during dwell stage of high-pressure spark plasma sintering. *Acta Mater* 2020, **199**: 469–479.

[5] Coble RL. Preparation of transparent ceramic Al_2O_3. *Am Ceram Soc Bullet* 1959, **38**: 507–510.

[6] Prins R. On the structure of γ-Al_2O_3. *J Catal* 2020, **392**: 336–346.

[7] Krell A, Klimke J, Hutzler T. Advanced spinel and sub-μm Al_2O_3 for transparent armour applications. *J Eur Ceram Soc* 2009, **29**: 275–281.

[8] Nečina V. Transparent ceramics by cold sintering process–Challenges and opportunities. *J Eur Ceram Soc* 2025, **45**: 117519.

[9] Guo J, Guo HZ, Baker AL, *et al.* Cold sintering: A paradigm shift for processing and integration of ceramics. *Angew Chem Int Edit* 2016, **55**: 11457–11461.

[10] Gao J, Ding Q, Yan P, *et al.* Direct cold sintering of translucent gamma-Al_2O_3 ceramics. *J Eur Ceram Soc* 2024, **44**: 4225–4231.

[11] Hérisson de Beauvoir T, Estournès C. Translucent γ-AlOOH and γ-Al_2O_3 glass-ceramics using the cold sintering process. *Scripta Mater* 2021, **194**: 113650.

[12] Tang LQ, Huang ZY, Deng M, *et al.* Densification of water-insoluble Li_2TiO_3 nanoceramics via a cold sintering process using water as a transient liquid phase. *J Adv Ceram* 2025, **14**: 9221133.

[13] Gao J, Wang KJ, Luo W, *et al.* Realizing translucency in aluminosilicate glass at ultralow temperature via cold sintering process. *J Adv Ceram* 2022, **11**: 1714–1724.

[14] Chen XT, Guo W, Wang HM, *et al.* Highly transparent cubic γ-Al_2O_3 ceramic prepared by high-pressure sintering of home-made nanopowders. *J Eur Ceram Soc* 2023, **43**: 4219–4225.

[15] Gallas MR, Piermarini GJ. Bulk modulus and Young's modulus of nanocrystalline γ-alumina. *J Am Ceram Soc* 1994, **77**: 2917–2920.

[16] Liao SC, Chen YJ, Kear BH, *et al.* High pressure/low temperature sintering of nanocrystalline alumina. *Nanostruct Mater* 1998, **10**: 1063–1079.

[17] Mishra RS, Lesher CE, Mukherjee AK. High-pressure sintering of nanocrystalline γAl_2O_3. *J Am Ceram Soc* 1996, **79**: 2989–2992.

[18] Ding JX, Guo J, Yan RJ, *et al.* Cold sintering process: A green route to fabricate thermoelectrics. *J Adv Ceram* 2024, **13**: 1697–1712.

[19] Chen XT, Hu JH, Chen GA, *et al.* Fabrication of highly transparent Y_2O_3–MgO nanocomposite ceramics in the visible-near-IR wavelength. *J Eur Ceram Soc* 2025, **45**: 117196.

[20] Guo HR, Shan YC, Zhang H, *et al.* A novel two-step sintering strategy for highly transparent AlON ceramics by combination of ultra-fast high-temperature sintering followed by conventional sintering. *J Adv Ceram* 2025, **14**: 9221182.

[21] Apetz R, van Bruggen MPB. Transparent alumina: A light-scattering model. *J Am Ceram Soc* 2003, **86**: 480–486.

[22] Ikesue A, Aung YL, Taira T, *et al.* Progress in ceramic lasers. *Annu Rev Mater Res* 2006, **36**: 397–429.

[23] Kang SL, Zhao XT, Guo J, *et al.* Evolution from transparent SiO_2 glass to ceramics enabled by cold sintering with a transient chemistry: H_2SiO_3. *Scripta Mater* 2023, **233**: 115522.

[24] Chen JC, Sharapa D, Plessow PN. Stability and formation of hydroxylated α–Al_2O_3(0001) surfaces at high temperatures. *Phys Rev Res* 2022, **4**: 013232.

[25] Ito S, Umehara N, Takata H, *et al.* Phase transition of γ-Al_2O_3 under hot isostatic pressure. *Solid State Ionics* 2004, **172**: 403–406.

[26] Ravenelle RM, Copeland JR, Kim WG, *et al.* Structural changes of γ-Al_2O_3-supported catalysts in hot liquid water. *ACS Catal* 2011, **1**: 552–561.

[27] Ze HJ, Yang ZL, Li ML, *et al. In situ* probing the structure change and interaction of interfacial water and hydroxyl intermediates on $Ni(OH)_2$ surface over water splitting. *J Am Chem Soc* 2024, **146**: 12538–12546.

[28] Gallas MR, Hockey B, Pechenik A, *et al.* Fabrication of transparent γ-Al_2O_3 from nanosize particles. *J Am Ceram Soc* 1994, **77**: 2107–2112.

[29] Zhao ZC, Xiao D, Chen KZ, *et al.* Nature of five-coordinated Al in γ-Al_2O_3 revealed by ultra-high-field solid-state NMR. *ACS Central Sci* 2022, **8**: 795–803.

[30] Dong JS, Wang J, Shi L, *et al.* Hydrogenous spinel γ-alumina structure. *Phys Chem Chem Phys* 2017, **19**: 27389–27396.

[31] Mo YF, Li CL, Li HY, *et al.* Hydrothermal stability of gamma-Al_2O_3 supports varied with crystal plane orientation of pseudo-boehmite precursor. *Chem Eng Sci* 2024, **287**: 119705.

[32] Grasso S, Biesuz M, Zoli L, *et al.* A review of cold sintering processes. *Adv Appl Ceram* 2020, **119**: 115–143.

[33] Jollands MC, Jin SY, Curti M, *et al.* Vibrational properties of OH groups associated with divalent cations in corundum (α-Al_2O_3). *Eur J Mineral* 2023, **35**: 873–890.